

KINEMATICS AND MASS MODELLING OF NGC 1068

WALTER DEHNEN

Theoretical Physics, Oxford

JONATHAN BLAND-HAWTHORN

Anglo-Australian Observatory

ANDREAS QUIRRENBACH

Max-Planck-Institut für Extraterrestrische Physik

AND

GERALD N. CECIL

University of North Carolina

Abstract. We present the kinematics of the ionized gas over the inner $140''$ (10 kpc) from observations with the HIFI Fabry-Perot interferometer. There is clear evidence for density wave streaming and bar-driven streaming across the field, with bi-symmetric arms that penetrate to within 200 pc of the nucleus. CO maps show linear structures along (although slightly offset from) the bar consistent with a strong shock. Along the spiral arms which encircle the bar, the H II regions lie downstream of the CO gas in the rest frame of the bar, as do the dust lanes, only if the gas outruns the stellar bar. As a first step towards understanding the details of the gas kinematics, and attempting to determine the mass inflow rate towards the nucleus, we build a mass model for the central disk constrained by near-infrared images. We plan to use this model as gravitational background potential for hydrodynamical simulations of the gas response to the bar. Comparing these with the data presented should enable us to constrain various quantities such as pattern speed, stellar mass-to-light ratio, central mass concentration, and gas fueling rate.

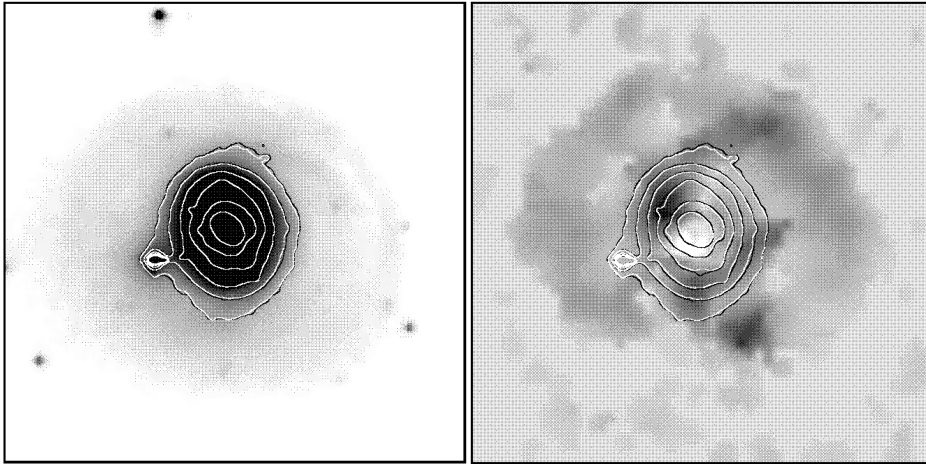


Figure 1. *Left:* (a) *B* band image of the outermost disk superimposed on *I* band contours. The field of view is $500''$ (37.5 kpc) sampled at $10'' \text{ pix}^{-1}$. *Right:* (b) VLA $\lambda 21\text{cm}$ observations (beam size $\approx 50''$ FWHM) of the distribution of atomic hydrogen throughout NGC 1068. The peak column density is $1.2 \times 10^{21} \text{ cm}^{-2}$; the column density falls below 10^{20} cm^{-2} beyond a radius of ≈ 18 kpc. Note the prevalent absorption in the nuclear regions, the dominant northern arm and the outer ring of hydrogen. *I* band isophotes have been superimposed (contoured) at equal log intervals with a resolution of $8''$ FWHM. A clear oval distortion is seen with $\text{PA} \approx 0^\circ$. The SE source is a saturated star.

1. Introduction

The luminous Seyfert 2 galaxy NGC 1068¹ lies at the forefront of attempts to unify the broader class of “active galaxies” within a single physical framework (Antonucci & Miller, 1985). Thus, it is surprising that so little is known of the large-scale gas motions in this nearby galaxy and, in particular, their connection with the nuclear activity.

2. Gas Kinematics

2.1. $\text{H}\alpha$ OBSERVATIONS

NGC 1068 was observed on the night of Dec. 8, 1985 using the Hawaii Imaging Fabry-Perot Interferometer (HIFI) at the CFH 3.6m telescope. The observations were made using an etalon with 85\AA free spectral range and a reflective finesse of 60. NGC 1068 was observed through two 50\AA FWHM blocking filters with central wavelengths $\lambda 6615$ and $\lambda 6585$ to cover $\text{H}\alpha$ and the neighbouring lines of $[\text{N II}]\lambda\lambda 6548, 6583$. Observations were also taken

¹Unless otherwise stated, global quantities for NGC 1068 are taken from the Ringberg Standard (Bland-Hawthorn *et al.*, 1997).

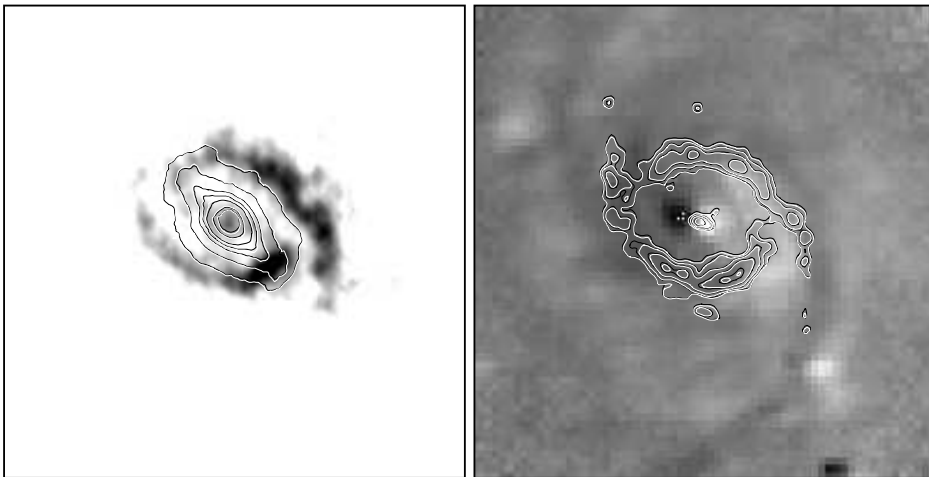


Figure 2. *Left:* (a) CO emission (Helfer & Blitz, 1995) superimposed onto the K band image of NGC 1068 (Thronson *et al.*, 1989) over a field of $100''$. The CO gas distribution is bi-symmetric about the nucleus, particularly along the bar, where it sits east of the bar axis to the northeast, and west of the bar axis to the southwest. *Right:* (b) CO emission (Planesas *et al.*, 1991) superimposed onto a B–I color image to emphasize that the cold gas sits *along the inside* of the dominant spiral pattern delineated by the optical arms (Sandage, 1961). This is particularly clear to the SW. The dark dust lane and optical arm correspond to $B-V \approx 1.0$ and $B-V \approx 0.5$ respectively (Ichikawa *et al.*, 1987).

for the $[\text{N II}]$ lines over the period Dec. 5–7, 1985 but cirrus and variable weather conditions have compromised these data. The Fabry-Perot system is placed at the $f/8$ Cassegrain focus and has an output beam of $f/2$ after focal reduction. At the time of the observations, the best available imaging detector was the TI 512×512 3-phase CCD whose 15μ pixels subtend $0.43''$ on the sky giving a $220'' \times 220''$ field-of-view. The data have a velocity resolution of 65 km s^{-1} FWHM. The $\text{H}\alpha$ and blue $[\text{N II}]$ lines were sampled at 40 km s^{-1} , while the red $[\text{N II}]$ line was sampled more coarsely at 78 km s^{-1} . The etalon produces a total velocity coverage of $\sim 4000 \text{ km s}^{-1}$ free of order confusion although only half this range was observed. The spatial resolution of the data is $1''$ in regions of high signal-to-noise ratio (e.g. the starburst ring), and roughly $2''$ in the diffuse gas.

2.2. LARGE-SCALE STRUCTURE

Deep optical and H I images of NGC 1068 (Fig. 1) show an outer θ -shaped ring and a bright central disk with diameter $\sim 20 \text{ kpc}$ oriented perpendicular to the outer ring. The innermost I band contour has the same dimension as the stellar bar seen at K (Fig. 2). In Fig. 3, we present the velocity field for the ionized gas over the inner disk. The velocity field is shown

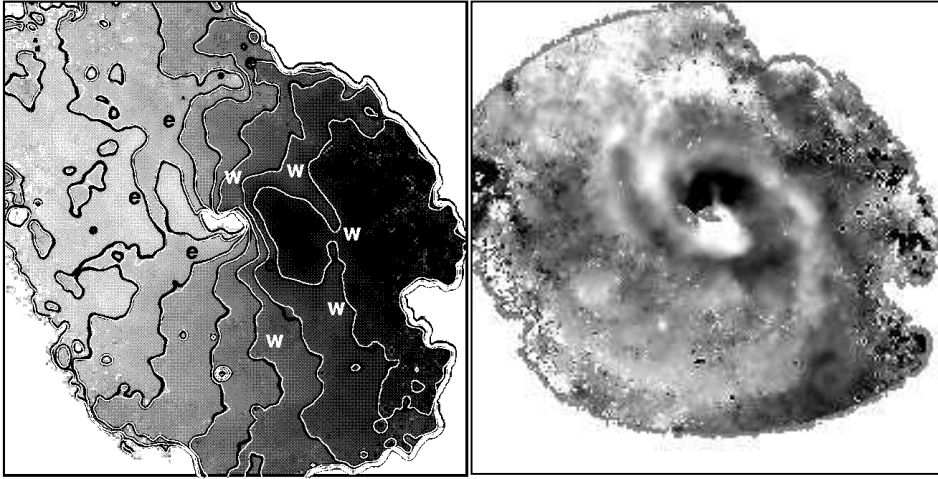


Figure 3. *Left:* (a) $H\alpha$ velocity field over the same field as Fig. 2. The contours from left to right correspond to -125 , -75 , -25 , 25 , 75 , and 125 km s^{-1} with respect to systemic velocity. Within the inner $40''$, the Z-shaped contours, characteristic of streaming along the bar, are well pronounced. This is particularly clear to the SW where the extended narrow-line region is much fainter and therefore does not pollute the bar streaming. The “w” and “e” labels show how the western and eastern kinematic arms spiral out from the nucleus into the large-scale disk. The central hole arises from problems in line fitting within the extended narrow line region; the AGN falls at the western edge of this hole. *Right:* (b) The residual velocities after subtracting a rotating disk model produced from the $H\alpha$ rotation curve in Fig. 5. Streaming motions are seen over the entire field, being particularly strong along the bar and in the two kinematic “e” and “w” arms. The greyscale range is the same as in (a).

for a field of view of $100''$ and reveals a series of concentric “kinematic spiral arms” which appear superimposed on ordered, large-scale rotation. As shown in Fig. 5, the large-scale disk appears to undergo flat rotation beyond a radius of 1.5 kpc with a kinematic major axis that is consistent with the photometric position angle of the outer ring. Across the inner $40''$, the Z-symmetric velocity contours are the hallmark of highly radial orbits along a bar (e.g. Huntley 1978). Thus, the observed elliptic streaming is consistent with the presence of the stellar bar detected at near-infrared wavelengths (Scoville *et al.*, 1988; Thronson *et al.*, 1989).

2.3. OBSERVED KINEMATICS

In Fig. 3a, the velocity field of the ionized gas is derived from the weighted sum of the $H\alpha$ and $[\text{N II}]$ kinematics. NGC 1068 has probably the most completely observed velocity field of any barred spiral galaxy due to a ‘diffuse ionized medium’ which pervades the inner disk (Bland-Hawthorn *et al.*, 1991). The large-scale disk clearly undergoes ordered rotation. However, no-

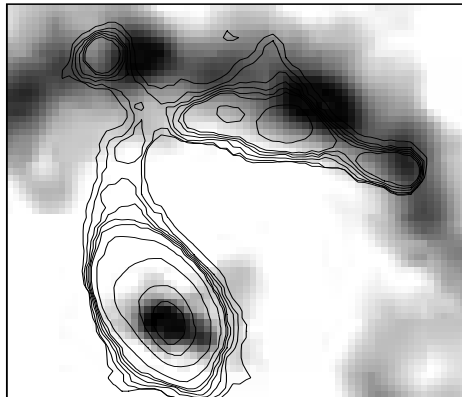


Figure 4. The $H\alpha$ flux map contoured over on the CO emission for a $25''$ field north of the nucleus. The “w” feature in (a) shows continuity in velocity along this feature, even across the CO spiral arms. Density wave action can be traced all the way into the narrow line region NE of the nucleus.

tice the bisymmetric streaming features $25''$ to the east and west of the nucleus, which are particularly apparent in the residual velocity field (Fig. 3b) after subtracting a rotating disk model. These are retarded with respect to the circular motion by 10 km s^{-1} on average reaching 30 km s^{-1} in places, which probably corresponds to 30 km s^{-1} up to 50 km s^{-1} in the plane of the galaxy. Additional kinematic spiral anomalies at larger radius are more diffuse. The characteristic Z-symmetry of an oval distortion (cf. Fig. 14 of Roberts *et al.*, 1979) can be traced all the way into the nucleus from the southwest, where the southeastern spiral feature is less noticeable. To the north, the spiral feature exhibits continuity in velocity as it crosses the elliptic ring. The western kinematic feature has a counterpart in the $H\alpha$ flux map (Fig. 4).

The $H\alpha$, H I (21 cm), and ^{12}CO ($J=1 \rightarrow 0$) rotation curves are presented in Fig. 5. There is good agreement between the CO (Helfer & Blitz, 1995) and the $H\alpha$ kinematics although rather less agreement with the H I data (VLA observations supplied by H. Liszt). However, the H I data use a $15''$ beam and the data have yet to be corrected for beam smearing and absorption in the centre. The velocity field shows extensive evidence for strong density wave streaming on all scales. In the $H\alpha$ data, there is a sharp transition region between $0''$ and $10''$ where the PA changes smoothly between 225° and 80° (Arribas *et al.*, 1996). A similar effect is seen in the H I data between $70''$ and $100''$ where the PA changes smoothly from 91° to 106° . For the $H\alpha$ and CO ring fits, the adopted inclination was 40° although the

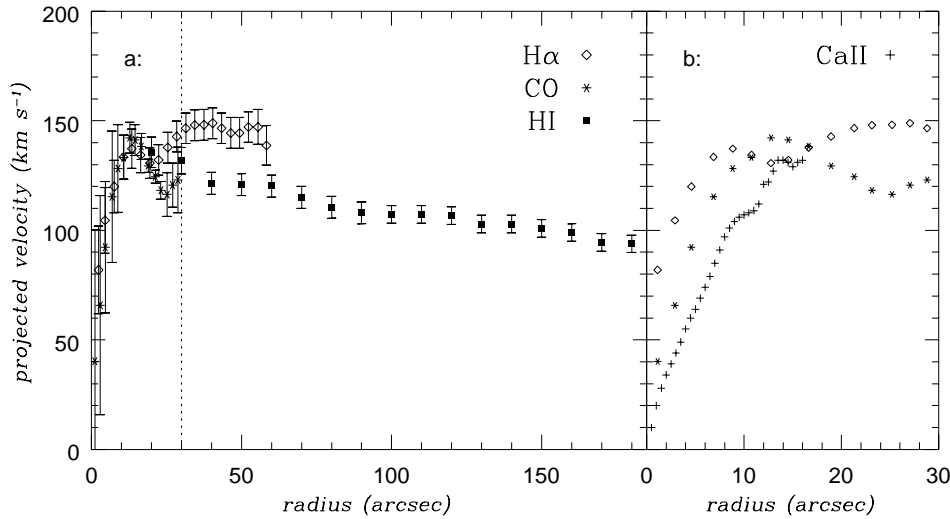


Figure 5. (a) Gas rotation curve observed in H α , CO and HI. (b) The points inside the dashed line in (a) have been blown up to show how H α and CO compare with the Ca II stellar velocities from García-Lorenzo *et al.* (1997). The absorption line measurements have typical uncertainties of $\pm 20 \text{ km s}^{-1}$.

orbit PA was a free parameter.

By subtracting the simple model of elliptic streaming overlaid on flat rotation, we have discovered bisymmetric spiral streamers in both the ionized line flux and kinematics that penetrate from ~ 1 kpc to within 100 pc of the AGN. We find evidence for this effect in both the CO line flux and kinematics, albeit at lower spatial resolution (Kaneko *et al.*, 1989). By implication, it is likely that the observed non-circular motions are confined to the galactic plane and arise from bar-driven density waves. In collaboration with Harvey Liszt (National Radio Astronomical Observatory), we find tentative evidence that, while the $\lambda 21\text{cm}$ and CO kinematics are largely consistent, the H α kinematics show substantial deviations from the cold phase at many positions within the inner disk away from the spiral streamers.

3. Mass Model

3.1. WHY WE NEED A MASS MODEL

Several studies of the gaseous response to rotating bar potentials can be found in the literature (e.g., Huntley *et al.*, 1978; Athanassoula, 1992). One of the main results is the occurrence of shocks at characteristic positions. One of these is an often tightly wound, trailing, and bisymmetric

spiral starting at both ends of the bar, exactly as observed for NGC 1068 (Fig. 2*b*). Associated with the shock is dust and cool gas visible in CO emission as spiral arms in Fig. 2*a*. Another place where shocks typically appear is along the bar usually somewhat offset from the major axis in the leading direction. For NGC 1068, Helfer & Blitz (1995) detected CO emission along the bar which indeed appears offset from the stellar bar's major axis towards the leading edge (Fig. 2*a*). Moreover, the models often have a central concentration of gas orbiting on near-circular, so-called x2-orbits, also evident in CO observations of NGC 1068. Thus, *qualitatively*, this fits nicely into the overall picture of the bar rotating prograde with respect to the disk.

However, theoretical studies also revealed a sensitive dependence of position and strength of the shocks to overall quantities such as pattern speed, bar strength, central mass concentration, and sound speed of the gas (Athanassoula, 1992; Englmaier & Gerhard, 1997). For a *quantitative* understanding of the gaseous morphology and kinematics in NGC 1068, a more detailed study is therefore highly desirable incorporating all information that is available on those quantities. In particular, the NIR light ought to be a good tracer of the underlying (stellar) mass distribution.

3.2. CREATING A MASS MODEL

Using NIR light as mass tracer to construct the gravitational potential for barred galaxies is by now a common technique (e.g., Quillen *et al.*, 1994). A little complication, which arises in the case of NGC 1068, is the presence of a central point source due to dust heated by the central AGN and emitting in the NIR. Here, we used three *K*-band images, (a) a very high-resolution ($0''.2$ FWHM) image of the centre, (b) a high-resolution image ($0''.4$ FWHM) of the stellar bar, and (c) a low resolution image ($2''$ FWHM) of the whole disk. The latter of these was supplied by H. Thronson (Thronson *et al.*, 1989), while images a and b were obtained with SHARP at the NTT (3.5m) using short exposures (0.1 and 0.5 seconds, respectively) in conjunction with a shift-and-add technique (Quirrenbach *et al.*, 1997).

A scaled PSF (an image of a star obtained under the same conditions) accounting for the point source was subtracted from image a, of which subsequently the azimuthally averaged luminosity profile was evaluated. To correct image b for the central point source, it was first split into non-axisymmetric and axisymmetric (azimuthally averaged) parts; second, inside $2''.8$ the latter was replaced by the profile obtained from image a; and finally, these were added back to the non-axisymmetric part. This procedure gave a high-resolution map of the stellar NIR emission inside $30''$. Finally, the map was extended with image c (though with lower resolution)

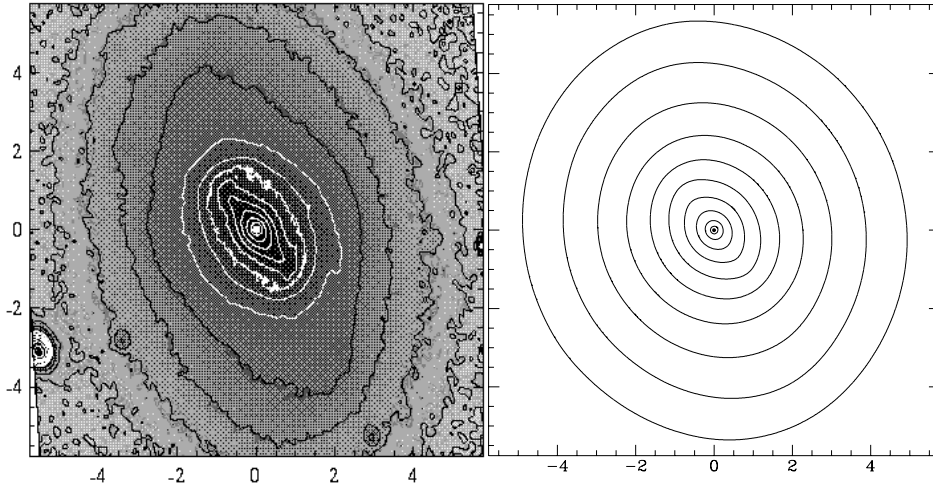


Figure 6. *Left:* (a) Density of our model (disk & bulge) in the plane of the galaxy ($z = 0$). Contours are spaced by 0.25 dex. Labels are in kpc. The bright star in the south-east does not enter the evaluation of the potential. Note that the angle between the major axes of inner bar and outer oval is smaller than it appears in projection (Fig. 1). *Right:* (b) Isocontours of the gravitational potential created by the density of disk and bulge, a black hole has not been added. Contours are spaced by 0.1 dex. The potential is both smoother and rounder than the mass distribution.

to $160'' \times 160''$ corresponding to $11.5\text{kpc} \times 11.5\text{kpc}$.

From this map a mass model was derived as follows: (i) a spherical model for the central (apparently round) bulge was subtracted; (ii) the remaining disk was de-inclined assuming $\text{PA}=106^\circ$ and $i=40^\circ$ (Bland-Hawthorn *et al.*, 1997); (iii) the resulting surface density was vertically thickened by the profile $(2h)^{-1} \exp(-|z|/h)$ with $h=200$ pc; and (iv) the spherical model for the central bulge was added back. Similarly, dark mass components such as a central black hole² and a halo may be added. The scale height of 200 pc is in agreement with a ratio of ~ 0.1 between scale height and length typical for disk galaxies in the infrared (Wainscoat *et al.*, 1989; Barnaby & Thronson, 1992).

Clearly, many parameters entering the above procedure are a priori not very well determined, e.g., the scale height and black hole mass. In particular, the dominance of the hot dust in the centre causes considerable uncertainty in the central stellar light distribution. Here we have used a γ -model (Dehnen, 1993) for the bulge component, the volume density of

²Presumably, in studies of the gas kinematics, a central point mass can hardly be distinguished from a very dense star cluster. However, the latter possibility might be ruled out by physical arguments (e.g. lifetime of such a cluster). Additional constraints on the central potential are given by maser kinematics (Greenhill *et al.*, 1996), though their interpretation is not straightforward.

which,

$$\rho_\gamma(r) = \frac{M(3-\gamma)}{4\pi} \frac{r_0}{r^\gamma(r+r_0)^{4-\gamma}}, \quad (1)$$

is proportional to $r^{-\gamma}$ for r much smaller than the scale radius r_0 and falls off as r^{-4} at large radii. Our parameters, $\gamma = 1.5$ and $r_0 = 0''.7$, are not well constrained by the K band photometry. For the future, we plan to improve on this point by taking into account also the J and H band which are less sensitive to emission from the hot dust in the centre. These data, in combination with the K image, may also be used to correct for dust absorption along the bar, which can be a problem particularly near the shocks.

The volume density in the plane of the galaxy resulting from this procedure is shown in Fig. 6a. As can be seen from the spacing of the contours, the scale length of the central bar is significantly smaller than that of the outer oval.

For gas kinematics and hydro-dynamical simulations, only the potential (and forces) in the plane $z=0$ are of interest. For the disk this has been evaluated from the expansion of the density in azimuthal harmonics up to order $m = 16$. The gravitational potential of the bulge model is given by

$$\Phi_\gamma(r) = -\frac{GM}{r_0} \times \begin{cases} \frac{1}{2-\gamma} \left[1 - \left(\frac{r}{r+r_0} \right)^{2-\gamma} \right] & \gamma \neq 2 \\ \ln \frac{r}{r+r_0} & \gamma = 2 \end{cases} \quad (2)$$

Fig. 6b shows isocontours of the potential due to disk and bulge.

In the future we plan to numerically evaluate the gaseous response to the mass model and compare the resulting gas distribution and kinematics with those observed (cf. the previous sections). Whether or not these data allow us to pin down all the unknown quantities (e.g., the central mass concentration) remains to be seen. However, the simulations published in the literature suggest that gas observation do – and thus *must* be used in order to – constrain these quantities.

4. Conclusions

In the context of standard spiral density waves, the expected large-scale shocks lead to a phase shift between the gas response and driving stellar bar. The resulting mass inflow may dominate standard viscous accretion. On much smaller scales, it is unlikely that such shocks can be sustained. Therefore, the shock mechanism is likely to be important at intermediate scales (0.1 to a few kpc). The mass inflow rate can then be computed

in terms of the gas properties, the underlying mass distribution, and the pattern speed. In future we shall attempt a self-consistent fit to these parameters, particularly the shock strength, which will require gas dynamic modeling. Ultimately, we would like to address the implications of these observations for fueling nuclear activity. A mass model is a precursor to running a full hydro-dynamical simulation.

Acknowledgements

We thank H. Liszt for allowing us to present unpublished VLA observations of the HI distribution, and B. García-Lorenzo who supplied the stellar velocities for Fig. 5. We would also like to thank H. Thronson for the large-scale *K* band image.

References

- Antonucci R.R.J. & Miller J.S. 1985, ApJ, 297, 621
 Arribas S., Mediavilla E. & García-Lorenzo B., 1996, ApJ, 463, 509
 Athanassoula E., 1992, MNRAS, 259, 345
 Barnaby D. & Thronson M.A., 1992, AJ, 103, 41
 Bland-Hawthorn J., Sokolowski J. & Cecil G. 1991, ApJ, 375, 78
 Bland-Hawthorn J., Gallimore J.F., Tacconi L.J., Brinks E., Baum S.A., Antonucci R.R.J. & Cecil G.N., 1997, this volume
 Dehnen W., 1993, MNRAS, 265, 250
 Englmaier P. & Gerhard O.E., 1997, MNRAS, 287, 57
 Friedli D., 1996, A&A, 312, 761
 García-Lorenzo B. *et al.*, 1997, this volume
 Greenhill L.J., Gwinn C.R., Antonucci R. & Barvainis R., 1996, ApJ, 472, L21; see also this volume
 Helfer T.T. & Blitz L., 1995, ApJ, 450, 90
 Huntley J.M., 1978, ApJ, 225, L101
 Huntley J.M., Sanders R.H. & Roberts W.W., 1978, ApJ, 221, 521
 Ichikawa S-I., Okamura S., Kaneko N., Nishimura M. & Toyama K., 1987, PASJ, 39, 411
 Kaneko N. *et al.* 1989, ApJ, 337, 691
 Planesas P., Scoville N. & Myers S.T., 1991, ApJ, 369, 364
 Quillen A.C., Frogel J.A. & Gonzales R.A., 1994, ApJ, 437, 162
 Quirrenbach A. *et al.*, 1997, this volume
 Roberts W.W., Huntley J.M., & van Albada G.D., 1979, ApJ, 233, 67
 Sandage A., 1961, Hubble Atlas of Galaxies, Carnegie Institute of Washington
 Scoville N.Z., Matthews K., Carico D.P. & Sanders D.B., 1988, ApJ, 327, L61
 Thronson H.A. *et al.*, 1989, ApJ, 343, 158
 Wainscoat R.J., Freeman K.C. & Hyland A.R., 1989, ApJ, 337, 163